Total column ozone climatology from MY34 to MY36 from measurements by the NOMAD-UVIS spectrometer

Conference or Workshop Item

TOTAL COLUMN OZONE CLIMATOLOGY FROM MY34 TO MY36 FROM MEASUREMENTS BY THE NOMAD-UVIS SPECTROMETER.

J.P. Mason, M.R. Patel, J.A. Holmes, P. Streeter, J. Alday, M. Brown, G. Sellers, C. Marriner, S.R Lewis, *School of Physical Sciences, The Open University, Milton Keynes UK (jon.mason@open.ac.uk)*, **M.J. Wolff,** *Space Science Institute, Boulder, CO, U.S.A*, **Y. Willame, C. Depiesse, B. Ristic, I. Thomas, F. Daerden, A.C. Vandaele,** *Royal Belgian Institute for Space Aeronomy BIRA-IASB* Belgium, **J.-J. Lopez-Moreno**, Instituto de Astrofisica de Andalucía/CSIC, Granada, Spain, **G. Bellucci,** Istituto di Astrofisica e Planetologia Spaziali, INAF, Rome, Italy.

Introduction: Near continuous radiance measurements of the martian atmosphere in the 200-650 nm wavelength range by the Ultraviolet and VISible spectrometer (UVIS) (Patel *et al*., 2017) as part of the NOMAD instrument on the ExoMars Trace Gas Orbiter (TGO) (Vandaele, *et al*., 2018) provides a powerful tool for investigating the ozone climatology, the water cycle (from the well-established photochemical anti-correlation between water vapour and ozone), and by extension photochemical reactions in the martian atmosphere.

Previous observations have shown that, spatially, ozone is observed in three main regions (1) at high northern latitudes (50° - 90° N) through the northern autumn, winter and spring seasons, (2) at equivalent high southern latitudes during the aphelion season, and (3) at low latitudes between 30°S - 30°N from L_s = 30° - 120°, coinciding with observations of the aphelion cloud belt (Bertaux *et al*., 2000; Clancy *et al*., 2016; Holmes *et al*., 2018). Entrapment of ozone in deep depressions, such as Hellas basin (Clancy *et al*., 2016), has been observed and associated with the meridional transport of O-rich air from northern latitudes and from south polar air being transported to equatorial regions after southern winter.

In this study, radiative transfer modelling, that includes multiple scattering from aerosols and surface reflectance, has been used to model the UVIS radiances in the wavelength range 220-310 nm to retrieve the O_3 column abundances for the latter half of Mars Year (MY)34 through MY36. We report the spatial distribution of ozone as measured by UVIS, including the observed entrapment and diurnal cycle of ozone within Hellas basin.

UVIS observations: TGO is in a near-circular 74° inclined orbit with a periapsis of 380 km and apoapsis of 420 km and an orbital period of approximately 2 hours allowing 12 dayside nadir passes per day. Full coverage of the surface achieved after 373 orbits (approximately 1 month) when the orbit 'closes' (repeats the same ground track). The repeatable ground track allows UVIS to make repeated measurements at the same location and because the orbit is not sun synchronous these measurements are at different local times.

The UVIS UV radiances suffer from a 'red-leak' with the majority of this straylight coming from wavelengths >650 nm. Accurate removal of this straylight has been achieved with the corrected UVIS radiances at 263 nm shown to be within ±15% of the MARCI band 6 radiances and within 10% at wavelengths of. 321 nm, 440 nm, 500 nm, and 600 nm corresponding to MARCI band 7, band 1 band 2, band 3 respectively (Mason *et al*., 2022).

Radiative transfer model: The radiative transfer is performed using the discrete ordinates DISORT package (Stamnes *et al*., 1988) and we employ the ''front-end'' routines (DISORT_MULTI) developed by M. Wolff, to generate the input grids and parameters required by DISORT (Clancy *et al*., 2003; Wolff *et al*., 2009, Wolff *et al*., 2010, Clancy *et al*., 2016, Wolff *et al*., 2019).

We use atmospheric fields outputted by the OpenMars atmospheric data set for Mars (Holmes *et al*., 2020) to define our *a priori* and atmospheric profiles. OpenMars uses the UK version of the Laboratoire de Météorologie Dynamique (LMD) Global Climate Model (GCM) (Forget *et al* 1999), which shares the same physical parameterisation schemes as the LMD model but uses a spectral dynamical core and an energy and angular momentum conserving vertical finite difference scheme. The model is coupled to a data assimilation scheme (Lewis *et al.* 2007) that interlaces observed values of temperature and dust into the model at each timestep. The assimilation used in this study incorporated temperature profiles and dust column data from the Mars Climate Sounder aboard the Mars Reconnaissance Orbiter (McCleese *et al*., 2007), as well as temperature profiles from the Atmospheric Chemistry Suite instrument aboard the ExoMars Trace Gas Orbiter (Fedorova *et al*., 2020). A priori profiles were constructed by linear interpolation of model output fields spatially and temporally to match the observation locations. In the vertical direction, the hypsometric equation was solved to map model sigma values into altitude coordinates prior to interpolation. A correction was applied to the model surface pressure fields in the hypsometric calculation, which accounted for the differences between the resolution-dependent model topographic dataset and the high-resolution Mars Orbiter Laser Altimeter (MOLA) topography dataset.

For the dust aerosol we employ the derived dust optical properties and phase functions from previous

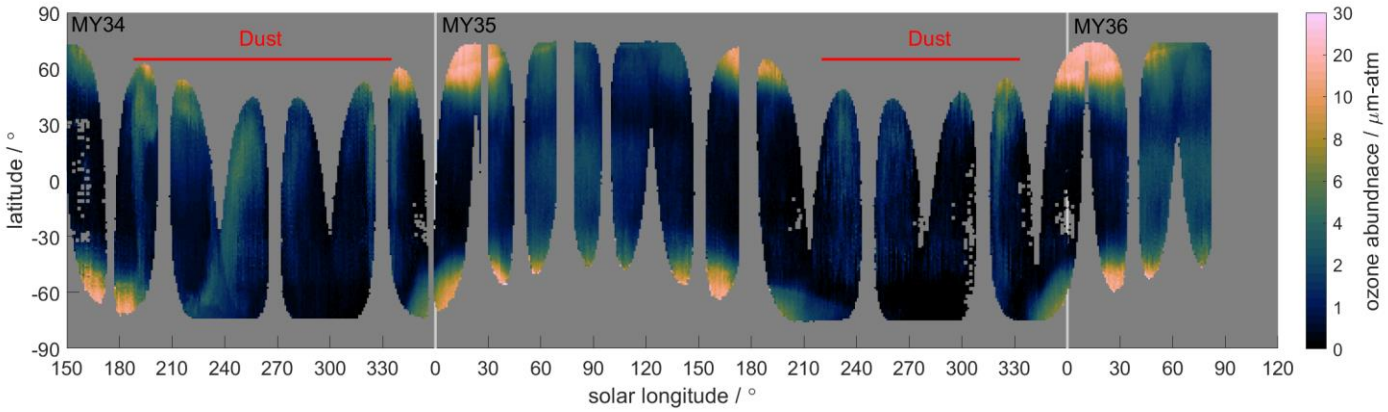

Fig. 1: The zonally averaged column abundances of O_3 as a function L_s and latitude over the period L_s = 150º (MY34) to L_s = 86º(MY36). Only observations with a solar zenith angle < 70º are shown and the 'Dust' labels indicate the periods where high dust loadings can result in false ozone detections.

studies (Wolff *et al*., 2010) and assume a single column average dust particle size distribution with moments of r_{eff} = 1.5 µm and v_{eff} = 0.1 µm. For water-ice clouds we use the optical scattering phase function of the droxtal shape ice particle following the retrievals for MARCI water-ice cloud retrievals (Wolff *et al*., 2019) and use a single size distribution described by the moments r_{eff} = 3.0 µm and v_{eff} = 0.1 µm. The optical properties of both the dust and water-ice particles at the UVIS wavelengths are found through linear interpolation and extrapolation from the MARCI wavelength bands.

In the nominal case, with a non-ice surface, the surface reflectance is described by an absorbing Hapke phase function and we use the Hapke UV reflectance map derived from MARCI and the CRISM data at 321 nm to obtain the relevant albedo at a given location (Wolff *et al*., 2019). By applying the same ratio between the derived albedos at 263 nm and 321 nm, linear interpolation and extrapolation are used to define the albedo across the 220-321 nm wavelength range. The coarse resolution of the albedo map in comparison to the UVIS spatial resolution can lead to inappropriate surface albedos for observations close to surface dichotomies. In our retrievals we address this fact by allowing the surface albedo to vary within 30% of the mapped values. If an ice surface is suspected, then the surface scattering is assumed to be Lambertian.

Retrieval procedure. Computation limitations restrict the number of wavelengths we can fit, therefore we chose to fit a total of 7 wavelengths [220, 230, 245, 250, 255, 304, 310] nm, the shorter two wavelengths are to provide sensitivity to the dust opacity, the longer wavelengths to determine the cloud optical depth, and the three wavelengths in the Hartley band to provide the ozone abundance. We use the MPFIT least squares routine to minimise the difference between the model and measured radiances by iterating the retrieved parameter: the albedo at 320 nm, dust optical depth, ice optical depth and ozone column abundance.

***Ozone climatology*:** The seasonal variation of ozone in MY34 through to MY36 is shown in Fig. 1. The characteristic and repeatable O_3 distribution is in agreement with previous measurements by SPICAM and MARCI (Bertaux *et al*., 2000; Clancy *et al*., 2016). The largest ozone abundances, in excess of 30 µm-atm, are observed in the colder and dryer spring, winter and autumn seasons in both hemispheres associated with lower solar radiation and low atmospheric water vapour content (Crismani *et al.*, 2021). The lower solar flux and the reduced available water vapour, reduces the production HOx and hence decreases the O_3 destruction rate from HOx reactions. The lack of O_3 retrievals poleward of 75° is a result of the ~74º inclined orbit of TGO, preventing observations of polar regions. We also only use observations with a solar zenith angle < 70° to ensure good observation signal.

The warmer perihelion season (L_s = 210°– 330º), with increased atmospheric water content and solar insolation sees ozone abundances reaching a minimum, typically around 1 µm-atm from -74 S to 50 N. It should be noted that ozone abundances around perihelion are at the UVIS detection limit, typically between 1 - 2 µm-atm dependent on the illumination conditions, namely the solar zenith angle. Another aspect of the perihelion ozone retrievals is the contamination by dust which results in erroneously high ozone abundances and is keenly seen in MY34 during the global dust storm (GDS) and to a lesser extent in MY35. The 'dust' labels in Fig. 1 indicates the periods where high dust loadings affect the ozone retrieval. The erroneous ozone resulting from high atmospheric dust loading is mainly a result of assuming a single dust particle size. Analysis of sky brightness measurements from the Curiosity Rover have shown that during the GDS the dust particle size rapidly increased to > 3 µm (Lemmon *et al*., 2019), likely resulting in larger dust particles higher in the atmosphere modifying the absorption and scattering characteristics of the dust.

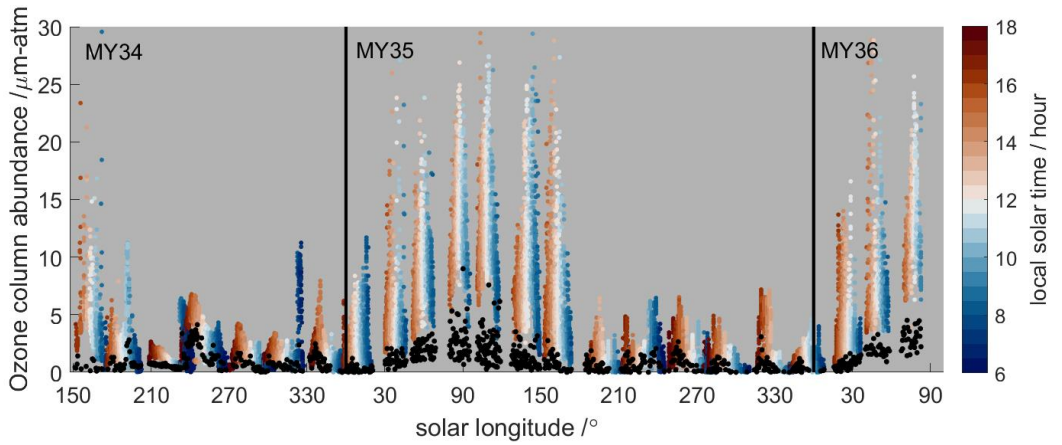

Fig. 2: The retrieved ozone abundances inside (colour) and outside (black) Hellas Basin from Ls = 148º (MY34) to Ls = 86º (MY36). The local solar time of each observation within Hellas is represented in the color scale.

In both MY35 and MY36 an ozone enhancement is observed at mid-latitude beginning around L_s = 30º and ending around L_s = 120º (MY35) in agreement with previous measurements from MY29-32 (Clancy *et al*., 2016). The enhancement extends from -30 S to 30 N, with ozone values between 2-4 µm-atm in the southern hemisphere and lower ozone abundances in the 0-30N region likely from the influx of water vapour from the north polar region. The ozone enhancement coincides with a cooling atmosphere and a lower hygropause (the altitude at which water vapour condenses). The lower condensation altitude suppresses the water vapour and by extension the formation of HO_x at higher altitudes allowing ozone to form. The dissipation of the aphelion ozone band precedes the decay of the aphelion cloud belt, likely a result of H_2O rich air from the sublimating southern pole being transported towards equatorial latitudes and an increasingly higher hygropause.

***Ozone entrapment*:** As we show in Fig. 2 ozone abundances in Hellas basin are enhanced throughout the reported period. Peak abundances >20 µm-atm are seen between L_s = 30° – 175° in MY35 and the beginning of an equivalent maximum can be seen at the start of MY36. The ozone within Hellas appears to decrease abruptly from L_s = >175° in both MY34 and MY35, however ozone levels remain enhanced throughout the rest of the year compared to the surrounding plain with abundances peaking between 4-6 µm-atm within Hellas and between 1-2 µm-atm outside Hellas.

Diurnal cycle. A key characteristic of the UVIS observations is the sampling of different local solar times (LST) which is represented in Fig. 2 by the colour scale. In the period L_s = 30°–175°, the peak ozone abundances are observed at noon(white) whereas by comparison the higher ozone columns are seen in either the morning (blue) or evening (red) between L_s = 175°-330° with perhaps a bias towards higher abundances in the evening. The diurnal cycle within Hellas is shown in Fig. 3 for two periods (a) between L_s = 220°-265° during perihelion and lower ozone and (b) between L_s = 80°-120° at the time of the observed peak in Hellas O_3 abundances. The colour bar represents the solar zenith angle as a proxy for the illumination conditions for each retrieval. The amount of incident sunlight is critical given the destruction pathway of O_3 from photochemical reactions. During both periods significant variation in the ozone abundance is observed within Hellas.

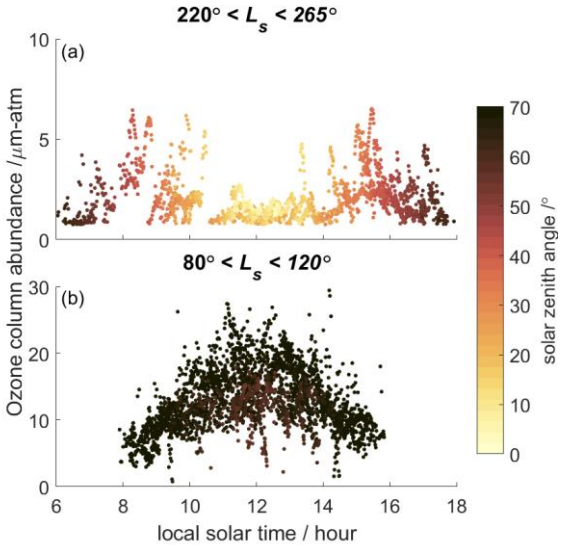

Fig. 3: The ozone diurnal cycle in the Hellas Basin for two period (a) L_s = 220°-265° and (b) L_s = 80°-120°. The colour scale shows the solar zenith angle for each observation to provide a representation of brightness.

For the perihelion period the O_3 abundance initially increases from 6am and is observed to peak in the mid-morning between 8-10am before abruptly decreasing just after 10am. A minimum in O_3 prevails from 10am to near 2pm, when the sun is at its zenith, before increasing again through mid-afternoon. In-

terestingly a peak in O_3 around 3pm is observed with slightly reduced abundance during the evening. By contrast the diurnal cycle in the period L_s = 80°-120° shows a steady increase in O_3 abundance through the morning from ~5 μm-atm to a peak around 12pm of ~25 μm-atm before a gradual decline back to ~5 μm-atm in the evening. As Fig 3 shows, during aphelion, the Sun remains low on the horizon around Hellas limiting the amount of O_3 loss through photolysis, however, a suppression in the peak ozone abundance is observed when the $\theta_z < 55°$.

References:

Bertaux, *et al*. (2000) "The study of the Martian atmosphere from top to bottom with SPICAM light on Mars Express." Planetary and Space Science 48.12-14: 1303-1320.

Crismani, *et al*. (2021) "A global and seasonal perspective of Martian water vapor from ExoMars/NOMAD." Journal of Geophysical Research: Planets 126.11: e2021JE006878.

Clancy, *et al*. (2016) "Daily global mapping of Mars ozone column abundances with MARCI UV band imaging." Icarus 266: 112-133.

Holmes, *et al*. (2018) "A reanalysis of ozone on Mars from assimilation of SPICAM observations." Icarus 302: 308-318.

Holmes, *et al*. (2020) "OpenMARS: A global record of martian weather from 1999 to 2015." Planetary and Space Science 188: 104962.

Fedorova, *et al*. (2020) "Stormy water on Mars: The distribution and saturation of atmospheric water during the dusty season." Science 367.6475: 297-300.

Forget, *et al*. (1999) "Improved general circulation models of the Martian atmosphere from the surface to above 80 km." Journal of Geophysical Research: Planets 104.E10: 24155-24175.

Lemmon, *et al*. (2019) "Large dust aerosol sizes seen during the 2018 Martian global dust event by the Curiosity rover." Geophysical Research Letters 46.16: 9448-9456.

Lewis, *et al*. (2007) "Assimilation of thermal emission spectrometer atmospheric data during the Mars Global Surveyor aerobraking period." Icarus 192.2: 327-347.

Mason, *et al*. (2022) "Removal of straylight from ExoMars NOMAD-UVIS observations." Planetary and Space Science: 105432.

McCleese, *et al*. (2007) "Mars Climate Sounder: An investigation of thermal and water vapor structure, dust and condensate distributions in the atmosphere, and energy balance of the polar regions." Journal of Geophysical Research: Planets 112.E5.

Patel, *et al*. (2017) "NOMAD spectrometer on the ExoMars trace gas orbiter mission: part 2—design, manufacturing, and testing of the ultraviolet and visible channel." Applied optics 56.10: 2771-2782.

Stamnes, *et al*. (1988) "Numerically stable algorithm for discrete-ordinate-method radiative transfer in multiple scattering and emitting layered media." Applied optics 27.12: 2502-2509.

Vandaele, *et al*. (2018) "NOMAD, an integrated suite of three spectrometers for the ExoMars trace gas mission: Technical description, science objectives and expected performance." Space Science Reviews 214.5: 1-47.

Wolff, *et al*. (2009) "Wavelength dependence of dust aerosol single scattering albedo as observed by the Compact Reconnaissance Imaging Spectrometer." Journal of Geophysical Research: Planets 114.E2.

Wolff, *et al*. (2010) "Ultraviolet dust aerosol properties as observed by MARCI." Icarus 208.1: 143-155.

Wolff, *et al*. (2019) "Mapping water ice clouds on Mars with MRO/MARCI." Icarus 332: 24-49.